

OPEN ACCESS

Tracing Low Amounts of Mg in the Doped Cathode Active Material LiNiO_2

To cite this article: Daniel Weber *et al* 2022 *J. Electrochem. Soc.* **169** 030540

View the [article online](#) for updates and enhancements.



Tracing Low Amounts of Mg in the Doped Cathode Active Material LiNiO₂

Daniel Weber,^{1,*,z} Jing Lin,^{1,=} Anuj Pokle,² Kerstin Volz,² Jürgen Janek,^{1,3} Torsten Brezesinski,¹ and Matteo Bianchini^{1,4,a,*,z}

¹Battery and Electrochemistry Laboratory, Institute of Nanotechnology, Karlsruhe Institute of Technology (KIT), Hermann-von-Helmholtz Platz 1, 76344 Eggenstein-Leopoldshafen, Germany

²Materials Science Center & Department of Physics, Philipps-University Marburg, Hans-Meerwein-Str. 6, 35032 Marburg, Germany

³Institute of Physical Chemistry & Center for Materials Research, Justus-Liebig-University Giessen, 35392 Giessen, Germany

⁴BASF SE, Carl-Bosch-Str. 38, 67056 Ludwigshafen, Germany

The resurgence of electromobility drives the need for high energy density cathode materials. LiNiO₂ (LNO) meets this demand, based on its high specific capacity in a narrow voltage range and without relying on scarce elements. Yet, it has been plagued by various issues, such as poor cycling performance and thermal instability. Adding dopants, such as widely available Mg²⁺, is a common strategy to balance cycling performance and energy density. Most prior studies focused on large Mg content ranges and were based on laboratory X-ray diffraction. Hence, the influence of Mg²⁺ addition on the crystal structure remains ambiguous, especially when small amounts are used (≤ 5 mol%; particularly interesting for industrial applications). Here, we present a systematic study of LiNi_{1-y}Mg_yO₂ ($0 \leq y \leq 0.05$) investigated by high-resolution synchrotron-based X-ray diffraction combined with elemental analysis, electron microscopy and electrochemical testing. The synthetic route relies on the addition of 10 nm Mg(OH)₂ nanoparticles prior to the final calcination, as well as on co-precipitation. It is found that Mg²⁺ mostly occupies the Ni site until saturating at $\sim 1.7\%$, then the Li site becomes preferred. This trend in the site occupancies influences the lattice parameters, oxygen coordinate within the unit cell and Ni–O bond distances. Doping also modifies the electrochemical behavior as a cathode material, stabilizing the capacity retention during cycling but sacrificing specific discharge capacity. Laboratory-based *operando* X-ray diffraction reveals that the increase in capacity retention is due to the suppression of the H2-H3 phase transition and interlayer distance collapse already in 3% Mg-doped LNO. The combination of structural and electrochemical characterization of doped LNO provides useful insights into the structural chemistry of the Mg²⁺ dopant and can serve as a starting point to understand Mg as a component in multiple dopant strategies for cathode material design and application.

© 2022 The Author(s). Published on behalf of The Electrochemical Society by IOP Publishing Limited. This is an open access article distributed under the terms of the Creative Commons Attribution 4.0 License (CC BY, <http://creativecommons.org/licenses/by/4.0/>), which permits unrestricted reuse of the work in any medium, provided the original work is properly cited. [DOI: 10.1149/1945-7111/ac5b38]



Manuscript submitted December 10, 2021; revised manuscript received March 2, 2022. Published March 23, 2022.

Layered cathode active materials (CAMs) for lithium-ion batteries based on LiNi_{1-x-y}Co_xMn_yO₂ (NCM) are enabling electromobility,¹ which necessitates a high energy density as well as excellent cycling stability. To meet the first demand, the amount of redox active Ni is constantly increased while the fraction of expensive Co and stabilizing Mn is decreased, leading to convergence towards LiNiO₂ (LNO).^{2,3} The pure LNO phase has a theoretical specific capacity of 275 mAh g⁻¹, which comes at the cost of a reduced cycling stability due to the instability of the Ni–O bond in the delithiated state of the material.^{4,5} In practice, the current record for the initial specific discharge capacity is at 245 mAh g⁻¹ in LNO, yet the material also exhibits problems typical of high Ni materials, such as the large capacity losses of 31% or more within the first 100 cycles.⁶ This strong degradation is caused primarily by the deep delithiation that can be achieved in LNO, resulting in oxygen evolution and subsequent structural collapse at the LNO particles surface (rock salt-type structure rearrangement).^{7–10} Thus, while LNO fulfills all the requirements in terms of energy density, low cost, and high operating voltage, the use of doping (elemental substitution with small amount of substitutional elements) is indispensable for performance stabilization.¹¹

One popular, low-cost dopant is the redox-inactive Mg²⁺ ion. Its stabilizing effect on the capacity retention was reported in various studies on LiNi_{1-y}Mg_yO₂ with y up to 0.5 in polycrystalline and μ m-sized single-crystalline materials.^{11–18} For example, $\sim 97\%$ capacity retention could recently be achieved for y = 0.05 at C/5 rate after 50

cycles.¹³ In addition to a high capacity retention, Mg-doped LNO also increases safety as evidenced by a shift of the reaction onset between the delithiated CAM with the electrolyte towards higher temperatures in accelerated rate calorimetry.¹⁵ Current investigations on dual doping strategies of 2% Mg with 2% Mn or Ti also show smoother voltage profiles, enhanced structural stability, elevated self-discharge resistance, and inhibited Ni dissolution.^{19,20} Also, the combination of 0.5% Mg and 0.3% Cu in LNO shows increased specific energy and cycle life due to bulk and surface stabilization.²¹ However, it should be noted that first principles calculations suggest Mg would not be an effective dopant to mitigate O₂ evolution from LNO, as well as the related rock salt-like structure formation at the surface.²² Thus, the stabilizing effect of Mg should be sought for elsewhere.

Initial studies based on laboratory powder X-ray diffraction (PXRD) traced the increased stability to Mg occupying the Li site (Mg_{Li}) in products synthesized from co-precipitated Ni_{1-y}Mg_y(OH)₂.¹² There, it was hypothesized that Mg acts as a pillar against the collapse of the interlayer space at high degrees of delithiation. As this collapse is associated with mechanical particles fracture, as well as with O₂ evolution and leads to hazardous side reactions with the organic electrolyte, even 2 to 5% of doping already leads to improved structural and mechanical stability, decreased CAM-electrolyte reactivity and increased safety in the delithiated state.¹⁵ Yet, this understanding was mostly developed based on large Mg contents > 5 mol%. When the Mg concentration is lower, assignment of the Mg occupancy to either the Li or Ni crystallographic site remains challenging, as laboratory diffraction data is often employed. Because the ionic radius of Mg²⁺ ($r = 0.72$ Å) lies between the radii of Li⁺ ($r = 0.76$ Å) and Ni³⁺ ($r = 0.56$ Å), ambiguity remains.^{12,23} In addition, two current dual doping studies combining PXRD and neutron diffraction suggest that Mg²⁺ prefers the Li site in the presence of Mn⁴⁺, but resides on the Ni site when co-doped with Ti⁴⁺.^{19,20} Hence, there is a gap in

*These authors contributed equally.

*Electrochemical Society Member.

^aPresent Address: Faculty of Biology, Chemistry and Geosciences & Bavarian Center for Battery Technology (BayBatt), University of Bayreuth, 95447 Bayreuth, Germany.

^zE-mail: daniel.weber3@kit.edu; matteo.bianchini@uni-bayreuth.de

understanding due to the lack of high-resolution data on the Mg-doped LNO.

Here, we synthesize a series of $\text{LiNi}_{1-y}\text{Mg}_y\text{O}_2$ samples in the doping regime of $y \leq 0.05$ and aim at elucidating the structure-property relationship. Toward this goal, we utilize high-resolution synchrotron radiation combined with inductively coupled plasma-optical emission spectroscopy (ICP-OES) and test different structural models to locate Mg in the structure. To maintain similar morphological properties and potentially relevant impurities content, doping is achieved by the use of $\text{Mg}(\text{OH})_2$ nanoparticles. The results are then validated using a sample prepared by the industrially relevant precipitation route. In combination with electrochemical testing and electron microscopy, this study complements previous findings and deepens the understanding of Mg as a single dopant element with great potential to stabilize the bulk structure of LNO.

Experimental

Materials synthesis.—Nominal $\text{LiNi}_{1-y}\text{Mg}_y\text{O}_2$ with $y = 0, 0.01, 0.017, 0.03, 0.05$ was synthesized from the starting materials $\text{Ni}(\text{OH})_2$ ($D_{50} = 11.8 \mu\text{m}$, BASF SE, Germany), $\text{LiOH}\cdot\text{H}_2\text{O}$ (BASF SE, Germany), $\text{Mg}(\text{OH})_2$ (10 nm particle size, 99% purity, US Research Nanomaterials Inc., USA), and co-precipitated $\text{Ni}_{0.983}\text{Mg}_{0.017}(\text{OH})_2$ (referred to as pCAM, $D_{50} = 12.2 \mu\text{m}$, BASF SE, Germany). The reactants were dry mixed in a laboratory blender for 30 min under Ar atmosphere in the required ratios with a 1 mol% excess of $\text{LiOH}\cdot\text{H}_2\text{O}$. The reactant mixtures were calcined in an alumina crucible under an O_2 flow of 2 volume exchanges per hour in a tube furnace (Nabertherm P330) with heating and cooling ramps of 3 K min^{-1} . A typical synthesis consisted of an intermediate annealing step at $500 \text{ }^\circ\text{C}$ for 12 h followed by a final annealing at $700 \text{ }^\circ\text{C}$ for 6 h. The samples were investigated by ex situ synchrotron PXRD, scanning electron microscopy with energy dispersive X-ray spectroscopy (SEM-EDS), elemental analysis, and electrochemical testing as coin cells vs Li metal anodes. Additionally, coin cells of LNO with 1.7% Mg and 3% Mg were investigated by operando PXRD during the first three cycles.

Synchrotron and operando PXRD.—Synchrotron PXRD patterns were measured at the Alba synchrotron at the Materials Science and Powder Diffraction beamline ($\lambda = 0.62001 \text{ \AA}$, $3.00\text{--}57.15^\circ 2\theta$ range).^{24,25} The data were collected using a one-dimensional Si-based position-sensitive MYTHEN detector in Debye-Scherrer geometry. The wavelength was calibrated to 0.62001 \AA using a Si standard from NIST. The instrumental contribution to the peak shape broadening was modeled via the Thompson-Cox-Hastings function and determined from a $\text{Na}_2\text{Ca}_3\text{Al}_2\text{F}_{14}$ (NAC) standard.

The diffraction data sets were analyzed using TOPAS Academic v6. In a typical refinement, intensities were extracted via a LeBail fit by refining the background as a set of Chebyshev (10 terms), lattice parameters, zero shift, axial divergence, hkl-dependent crystallite size based on the spherical harmonics approach²⁶ and microstrain. During Rietveld refinement, prior parameters were initially fixed and the oxygen z -coordinate (z_{O}), site occupancies and Debye-Waller factors (B_{iso}) refined while utilizing an absorption correction. In a final step, all parameters were refined in parallel until convergence was reached. The confidence intervals are given as the estimated standard deviations obtained from TOPAS multiplied by a factor of 3.

Operando PXRD was conducted on a STADI P (STOE) diffractometer in transmission geometry at room temperature utilizing monochromatic $\text{Mo-K}_{\alpha 1}$ radiation ($\lambda = 0.7093 \text{ \AA}$, $U = 50 \text{ kV}$, $I = 40 \text{ mA}$), a Mythen 1 K detector (Dectris), and a Gamry Interface 1000 potentiostat. Samples were introduced as half-cells vs Li foil in coin cells utilizing casings with glass window of 6 mm diameter and $160 \mu\text{m}$ thickness. The cell was cycled at a rate of C/10 while collecting XRD patterns simultaneously in the range $6^\circ < 2\theta < 37^\circ$ with a collection time of 10 min per pattern. Prior to the measurement, instrument parameters, such as slit width, a full axial

divergence model, and Thompson-Cox-Hastings pseudo-Voigt peak shapes, were determined from Si NIST 640 f sandwiched in an electrochemical cell.

Refinement of the *operando* data was performed in sequential order using the results from synchrotron PXRD refinement as the starting values for the CAM phase. The background was modeled using a six-term Chebyshev function. For the CAM phase, the scale factor, lattice parameters, B_{iso} , x & z coordinate of oxygen (x only in monoclinic phase), as well as a correction for sample absorption and sample displacement in transmission mode were refined. The site occupancy of Li was neglected due to its negligible X-ray scattering cross-section. Additionally, a secondary phase for the Al current collector was included in the refinement.

Elemental composition.—The elemental composition of the product was determined by ICP-OES using a Thermo Fischer Scientific ICAP 7600 DUO. Powder samples were dissolved in an acid digester in a graphite furnace. The mass fraction values were obtained by three independent measurements for each sample.

Electron microscopy.—SEM was carried out with a Leo 1530 SEM (Zeiss) equipped with a zirconia-coated tungsten filament working at an accelerating voltage of 10 kV with an in-lens SE detector. Maps of the elemental distribution were collected via EDS using an Oxford X-Max detector (Oxford instrument) at an acceleration voltage of 20 kV. Samples were prepared in an Ar atmosphere on adhesive carbon chips placed in the sample holders.

The scanning transmission electron microscope (STEM) sample cross-section was carried out by JEOL JIB 4601 F multibeam system operating at 1–30 kV for the electron and Ga-ion beam. To minimize air exposure, all the samples were stored in the glove box. The secondary particles were first coated by C coating using an e-beam assisted C/W deposition, followed by Ga-ion-assisted $3 \mu\text{m}$ thick W deposition. Starting with a 30 kV ion beam, a cross-sectional sample is fabricated by thinning down the lamella to $\sim 100 \text{ nm}$, where a 3 kV ion beam does the polishing. Finally, low-energy gentle milling (Fishione Model 1040 Nanomill) is performed using a 500 eV Ar-ion beam on both sides to remove any Ga-ion implantation and damaged/ amorphous layers. The STEM micrographs and EDS maps were obtained by a double Cs-corrected JEOL JEM-2200 FS operated at 200 kV with a 21 mrad convergence angle. STEM micrographs are HAADF (high-angle annular dark-field) images.

Electrochemical cell preparation.—Electrode tapes were prepared by casting a slurry containing CAM, conducting carbon, and a polymer binder in an organic solvent onto a metal-film current collector. The slurry was obtained by first mixing 1.01 g of a 7.5 wt % binder solution of polyvinylidene difluoride (PVDF, Solef 5130, Solvay) in *N*-methyl-2-pyrrolidone (NMP, >99.5%, Merck) with 0.8 g Super C65 (BASF) and 0.45 g NMP in a planetary centrifuge mixer (ARE250, Thinky) with two-step program (3 min at 2000 rpm, 3 min at 400 rpm). After adding 2.45 g of CAM to the slurry, the mixture was stirred again using the same program. The slurry was spread onto a 0.03 mm Al foil using an Erichsen Coatmaster 510 coating machine with coating rate 5 mm s^{-1} and a $120 \mu\text{m}$ slit. The resulting tapes were dried overnight at $120 \text{ }^\circ\text{C}$ in a vacuum and calendared at 15 N mm^{-1} (Sumet Messtechnik). After removal of the NMP, the electrodes had a mass ratio 94:3:3 (CAM:PVDF:Super C65). The active material loading was 10 mg cm^{-2} and tapes were stored under inert atmosphere. Coin cells were assembled using 12 mm diameter disc punched out of the calendared electrode tapes, LP57 electrolyte (1 M LiPF_6 in a mixture of ethylene carbonate and diethylene carbonate in a 3:7 weight ratio), GF/D separator (Whatman), and Li metal in an Ar glovebox.

Electrochemical testing.—The standard cycling performances were investigated on cells in a battery cycler (MACCOR Inc.) after a post-assembly equilibration time of at least two hours. Cycling was performed in the voltage range of 3–4.3 V vs Li^+/Li at $25 \text{ }^\circ\text{C}$. The

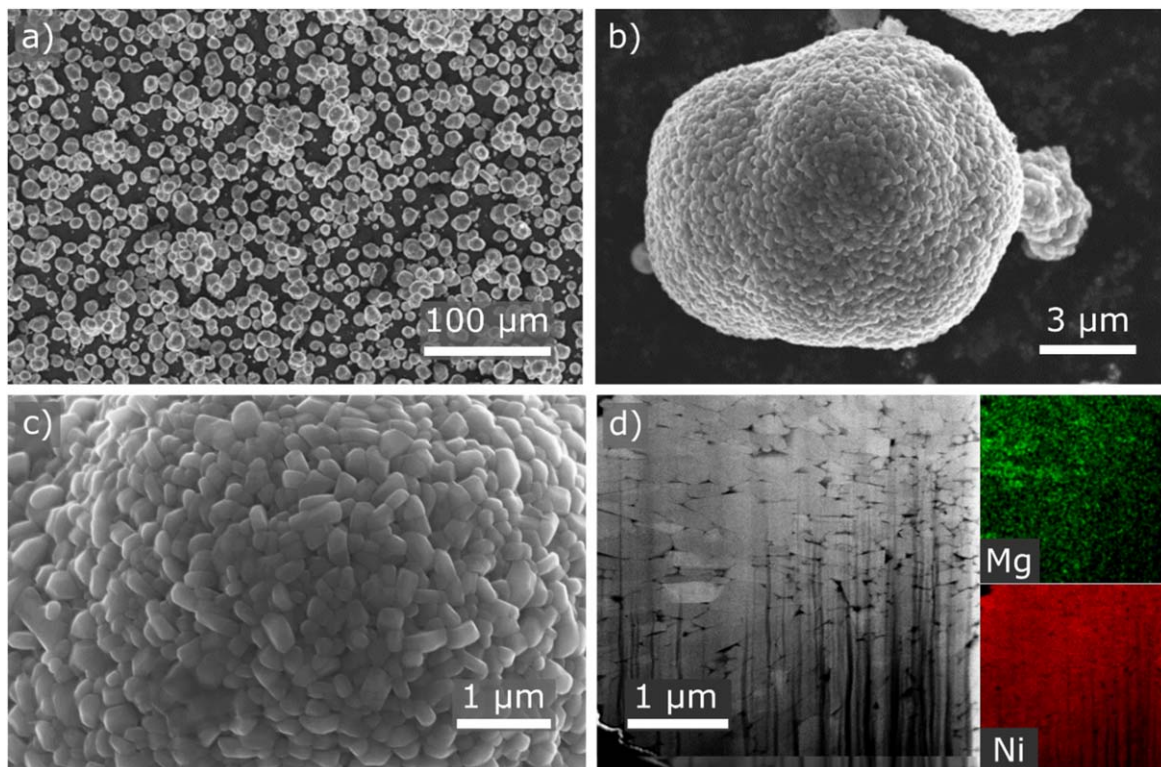


Figure 1. (a)–(c) SEM images of 1.7 mol% Mg-doped LNO at various magnifications, (d) FIB cut cross-section of a secondary particle (particle surface towards the right side) with STEM based EDS maps of Mg and Ni of the same region.

Table I. Metal content of all samples as probed by ICP-OES.

Mg _{nominal}	0%	1.0%	1.7%	3.0%	5.0%	1.7% (pCAM)
Li _{ICP}	1.00(2)	0.97(2)	0.97(2)	0.96(2)	0.95(2)	1.03(2)
Mg _{ICP}	0	0.0121(4)	0.0191(7)	0.031(1)	0.052(12)	0.0167(4)
Ni _{ICP}	1.00(1)	0.99(1)	0.983(13)	0.97(1)	0.95(1)	0.983(13)

half-cells were charged and discharged at a rate of C/10 (with 1C = 225 mA g⁻¹) for the first 5 cycles, followed by another 100 cycles at a rate of 1C. After every 50 cycles at 1C, charging and discharging with C/10 was performed to test the capacity compared to the initial cycle without impeding kinetic effects. At least three coin cells were assembled for the test of each CAM.

Results and Discussion

Synthesis.—In order to investigate the low doping range of Mg in LiNiO₂, samples were synthesized from spherical particles of Ni(OH)₂ ($D_{50} = 11.8 \mu\text{m}$) and 10 nm Mg(OH)₂ nanoparticles in the relevant ratios in the presence of bulk LiOH·H₂O (\geq mesh 250) with 1% excess via a solid-state reaction. Doping fractions of 0, 1, 1.7, 3, and 5 mol% Mg on the Ni site (as in LiNi_{1-y}Mg_yO₂) were chosen as the target compositions and will be used to denominate the samples throughout the text. The materials were mixed in a laboratory shear mixer for 30 min, pre-annealed, and then fired to the final temperature. Phase-pure, doped samples were accessible by utilizing highly reactive 10 nm Mg(OH)₂ nanoparticles as a Mg²⁺ source. The reactivity of the nanoparticles originates from their small size and activation via the dehydration to MgO. 100 nm Mg(OH)₂ nanoparticles did not result in single-phase products, but featured a rock salt-type side phase with a peak in the range of $\sim 16.9^\circ 2\theta$. The application of Mg(NO₃)₂ films deposited from isopropanol solution²⁷ also yielded either rock salt-type impurities or led to degraded electrochemical behavior compared to LNO:Mg from

10 nm Mg(OH)₂. In addition to doping via 10 nm particles, a Ni_{0.983}Mg_{0.017}(OH)₂ reactant was co-precipitated in BASF and lithiated in our lab (labeled here as pCAM) to investigate possible differences compared to the nanoparticle route. The descriptions in the manuscript refer to doped samples prepared via nanoparticles addition unless otherwise noted. The composition and morphology of the final products were investigated via ICP-OES and SEM-EDS. The ratios of the metal ions within the products based on ICP-OES are given in Table I and only show slight deviations from the nominal values of the Mg fraction. Figures 1a–1d displays exemplary and representative SEM and STEM-EDX images of the 1.7 mol % Mg-doped LNO at various levels of magnification. The secondary particles of all doping levels feature a spherical morphology with diameters ranging between 9 and 14 μm , without any observable particles of other morphologies. The secondary particles consist of primary particles with edge lengths that vary between 120 and 620 nm. Additionally, the cross-section of a single secondary particle prepared by focused-ion-beam (FIB) milling reveals a shrinking primary particle size towards the core of the secondary particle. SEM-EDS on the FIB cut sample shows a homogeneous elemental distribution of Mg and Ni across the material on the 10 s of nm scale with little to no clustering of Mg.

Synchrotron PXRD.—In order to locate the Mg dopant in the LNO unit cell, the crystal structures of all samples were investigated by synchrotron PXRD and subsequent Rietveld refinement. The diffraction patterns are very similar as displayed in Fig. 2a and

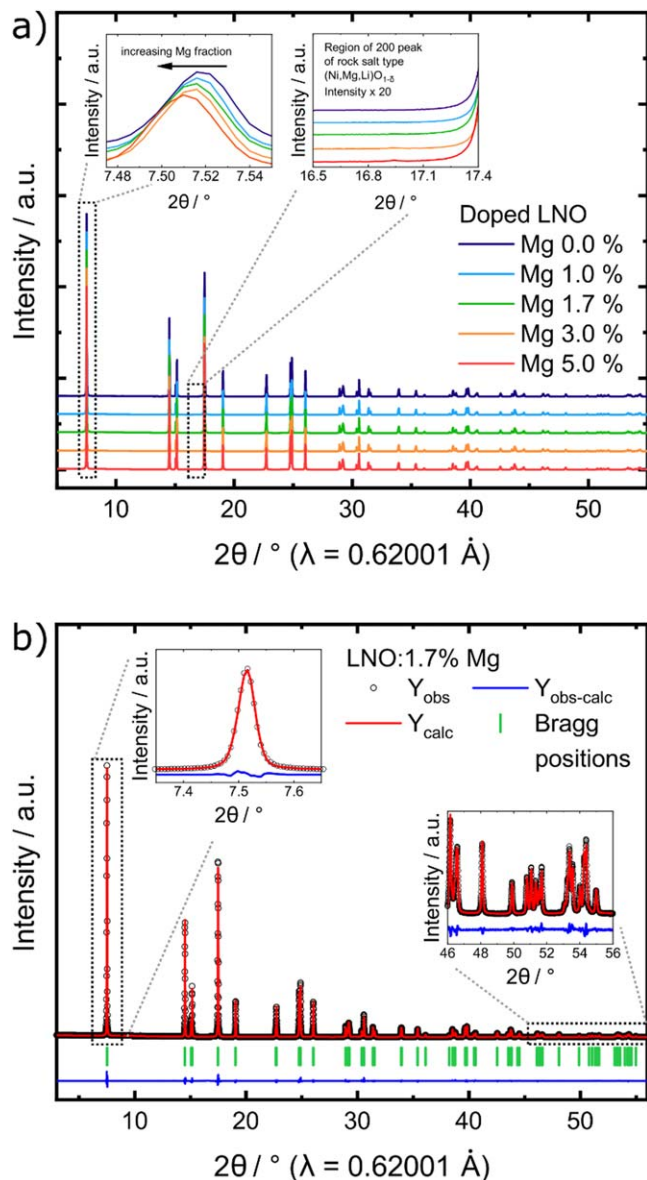


Figure 2. (a) Synchrotron PXRD patterns of LNO of various doping levels. Insets show the shift of the 003 peak with increasing Mg doping level, as well as the region typical of the 200 peak of the $(\text{Ni,Mg,Li})\text{O}_{1-\epsilon}$ rock salt-type phase at around $\sim 16.9^\circ$ in 2θ . (b) Exemplary overlay of observed and calculated patterns, difference curve, and ticks for the Bragg positions, with insets highlighting the quality of the fits on the 003 peak and the high-angle region.

feature subtle shifts of the peak positions with increasing doping level, as for example the decrease of the 003 peak with increasing Mg content. No significant amount of $(\text{Ni,Mg})\text{O}$ rock salt-type impurity was found, which usually exhibits a 200 reflection at $2\theta \approx 16.9^\circ$. The patterns were indexed in the hexagonal crystal system with unit cell lattice parameter a ranging from 2.87771(24) Å to 2.87876(24) Å and lattice parameter c ranging from 14.19726(17) Å to 14.21035(17) Å. The close agreement of observed and calculated pattern over the full 2θ range indicates the high quality of the Rietveld fit, as displayed for example in Fig. 2b for the data on 1.7 mol% Mg-doped LNO. Further details regarding the crystallographic data are summarized in Tables II and III, as well as plotted in Fig. 3. There, the lattice parameters show clear trends with the degree of doping. The lattice parameter a expands by the introduction of Mg^{2+} at 1 mol%, then shrinks for Mg^{2+} at 1.7 and 3 mol% and finally strongly increases at 5 mol% Mg^{2+} . In contrast, the

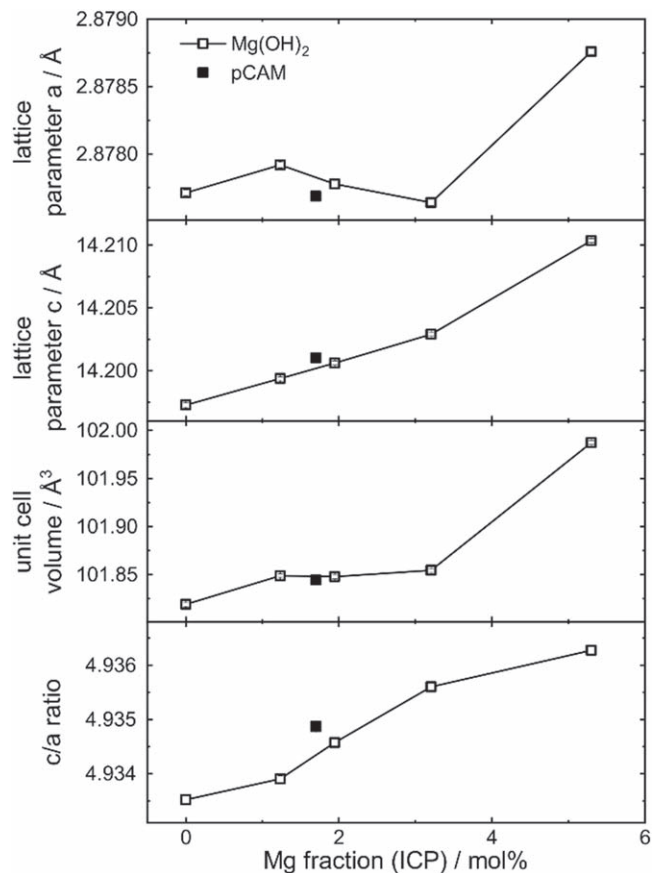


Figure 3. Lattice parameter a , c , the unit cell volume, as well as the c/a ratio vs the degree of doping as determined by ICP-OES. Error bars are within the symbols size.

lattice parameter c increases monotonically with increasing doping level, and the evolution of the volume is naturally formed by a superposition of the trends in both lattice parameters. The c/a ratio, a metric for the degree of layering in LNO and isostructural compounds,⁵ increases from 4.933 to 4.936 with increasing doping level. To model the anisotropy of the platelet-shaped primary particles, the crystalline domain size was modified by a spherical harmonics function of the 4th order and measured as the volume average column height. It ranged between 154 and 177 nm and no clear trend between domain size and degree of doping was observed. Additionally, the refinement of microstrain broadening on the order of $\epsilon_0 \approx 0.044$ to 0.047 further improved the fit between measured and calculated data.

In order to track changes within the unit cell with respect to the doping levels, the structural models were refined in the space group $R\bar{3}m$ with hexagonal indices while taking into account the sample absorption including a cylindrical sample form factor given by the Debye-Scherrer geometry.²⁸ The refinement included the z coordinate of oxygen (z_{O}), site occupancies of Li and Ni including occupational defects (see Table III), as well as the atomic displacement parameter (B_{iso}) for each site. As a high degree of homogeneity of Mg in LNO was observed in STEM-EDS and reported in prior studies,²⁰ the amount of Mg was constrained to the values obtained from ICP-OES and allowed to occupy either the Ni (Mg_{Ni}) and/or the Li site (Mg_{Li}). Additionally, in order to account for occupational defects of Ni^{2+} on the Li site (Ni_{Li}) commonly observed in pristine LNO, Ni_{Li} was refined and the total metal site occupancies constrained to 1. Thus, we account for the possibility of Mg^{2+} to distribute between the Ni and Li sites while in parallel taking into account the Ni^{2+} occupational defect. In summary, as gathered in Table III, the refinement contained 5 variable SOFs, Mg_{Ni} , Ni_{Ni} ,

Table II. Details on the results from Rietveld refinement for synchrotron PXRD of $\text{LiNi}_{1-y}\text{Mg}_y\text{O}_2$ performed at $T = 302$ K.

Mg/mol%	0	1	1.7	3	5	1.7 pCAM
Space group				$R\bar{3}m$		
$a/\text{\AA}$	2.87771(2)	2.87792(2)	2.87778(3)	2.87764(2)	2.87876(2)	2.87769(2)
$c/\text{\AA}$	14.19726(17)	14.19937(14)	14.20061(17)	14.20289(16)	14.21035(16)	14.20102(14)
$V/\text{\AA}^3$	101.819(2)	101.849(2)	101.848(2)	101.855(2)	101.987(2)	101.844(2)
c/a	4.93352(7)	4.93390(6)	4.93457(8)	4.93560(7)	4.93627(7)	4.93487(6)
z_{O}	0.25875(13)	0.25890(11)	0.25898(12)	0.25893(12)	0.25881(12)	0.25907(11)
$S/\text{\AA}$	2.118(4)	2.114(3)	2.112(4)	2.113(3)	2.118(3)	2.109(3)
$d(\text{Ni-O})$	1.9702(10)	1.9692(8)	1.9686(9)	1.9690(9)	1.9708(9)	1.9679(9)
Site occupancy Ni_{Li}	0.0247(18)	0.0232(3)	0.0214(3)	0.0203(3)	0.0202(2)	0.019(3)
Site occupancy Mg_{Li}	0*	0.000(8)	0.000(9)	0.012(9)	0.032(2)	0.000(8)
Site occupancy Mg_{Ni}	0*	0.012(8)	0.019(9)	0.020(9)	0.020(2)	0.017(8)
$B_{\text{iso}}(\text{Ni})$	0.311(10)	0.310(9)	0.305(10)	0.299(11)	0.303(10)	0.312(10)
$B_{\text{iso}}(\text{O})$	0.70(3)	0.71(4)	0.71(4)	0.66(4)	0.63(3)	0.71(4)
Mw/g/mol	98.9(5)	98.4(5)	98.1(5)	98.2(5)	98.5(5)	98.1(5)
R_{wp}	4.89	4.20	4.48	4.62	4.52	4.28
R_{Bragg}	1.17	1.19	1.17	1.29	1.38	1.29

Values marked with * were not refined.

Table III. Atomic coordinates with Wyckoff positions, as well as assignment of the site occupancy factors (SOF) and Debye-Waller factors (B_{iso}) for $\text{LiNi}_{1-y}\text{Mg}_y\text{O}_2$.

Atom	Wyckoff position	x	y	z	SOF	B_{iso}
Li	3b	0	0	$\frac{1}{2}$	$\text{Li}_{\text{Li}}^{\text{a}}$	$B_{\text{iso}}(\text{Li})$
Ni	3b	0	0	$\frac{1}{2}$	$\text{Ni}_{\text{Li}}^{\text{a}}$	$B_{\text{iso}}(\text{Li})$
Mg	3b	0	0	$\frac{1}{2}$	$\text{Mg}_{\text{Li}}^{\text{a}}$	$B_{\text{iso}}(\text{Li})$
Ni	3a	0	0	0	$\text{Ni}_{\text{Ni}}^{\text{a}}$	$B_{\text{iso}}(\text{Ni})$
Mg	3a	0	0	0	$\text{Mg}_{\text{Ni}}^{\text{a}}$	$B_{\text{iso}}(\text{Ni})$
O	6c	0	0	z_{O}	1	$B_{\text{iso}}(\text{O})$

a) Constraints: (1) $\text{Mg}_{\text{Ni}} + \text{Mg}_{\text{Li}} = \text{Mg}_{\text{ICP}}$, (2) $\text{Ni}_{\text{Ni}} + \text{Ni}_{\text{Li}} = 1$, (3) $\text{Mg}_{\text{Ni}} + \text{Ni}_{\text{Ni}} = 1$, (4) $\text{Mg}_{\text{Li}} + \text{Ni}_{\text{Li}} + \text{Li}_{\text{Li}} = 1$.

Mg_{Li} , Ni_{Li} , and Li_{Li} . Given that such a system would be over-parameterized, we added 4 constraints, as described above (total Mg content = Mg_{ICP} , total Ni content = 1, full occupancy of sites 3a and 3b). Models that place Mg on either the Li or Ni site were tested but found to yield higher values of R_{wp} and R_{Bragg} . Likewise, the ICP values were used only for the Mg content, as tests with constraints based on the Li and Ni ICP contents yielded negative Li SOF values, likely because ICP measured values also include minor side phases, such as Li residuals for example (Li_2CO_3 , LiOH), that are ubiquitous in Ni-rich CAMs.²⁹

The evolution of the described parameters with increasing Mg content is displayed in Figs. 4a, 4b. Doping with Mg^{2+} first leads to an increase in z_{O} and a shrinking of the Ni–O bond distance from $d(\text{Ni–O})$ of 1.9702(10) Å in pristine LNO to 1.9686(9) Å at 1.7 mol% Mg. The decreasing bond length can be rationalized by the motion of the oxide anions at (0 0 z_{O}) closer to the Ni ions at (2/3 1/3 1/3), which is symmetry equivalent to Ni at (0 0 0). The decreasing distance is not compensated by the evolution of the lattice parameters. The trend then reverses at doping levels beyond 1.7 mol% until $d(\text{Ni–O})$ of 1.9708(9) Å is reached at 5 mol% Mg doping. A similar trend is observed for the NiO_2 layer height (S), which is defined by the distance between the two layers of oxygen neighboring to the Ni plane according to $S = 2 \cdot c \cdot (1/3 - z_{\text{O}})$. The difference between the behavior of $d(\text{Ni–O})$ and of the stacking height S can be rationalized by taking into account the evolution of the lattice parameter a for $d(\text{Ni–O})$: in fact, $d(\text{Ni–O})$ is sensitive to the a parameter, while S is not.

The abovementioned monotonic trends in z_{O} , $d(\text{Ni–O})$, and S strongly correlate with the site occupancies of Ni_{Li} , Mg_{Ni} , and Mg_{Li} .

There, we observe that Mg first occupies the Ni site with up to 1.7% Mg_{Ni} . Additional Mg ($\text{Mg}_{\text{Li}} = \text{Mg}_{\text{ICP}} - \text{Mg}_{\text{Ni}}$) beyond 1.7% of total doping levels is found in the Li layer. The site occupancy of Ni_{Li} is relatively stable and varies from 2.5(2) % in pristine LNO to 2.0(2) % in LNO doped with 5 mol% Mg. We also observe a significant increase of the Mg_{Li} occupancy already at doping levels beyond 1.7 mol% in our samples. This partly agrees with previous studies, where increasing Mg amount was found on the Li site with increasing nominal Mg content, but at the same time, Mg on the Ni site was only found at high Mg content beyond 5 mol%. However, at the time synchrotron radiation was not used. Finally, the co-precipitated sample investigated here features a similar behavior to the samples doped via $\text{Mg}(\text{OH})_2$ nanoparticles. It should be noted that the observed error bars for Mg_{Ni} and Mg_{Li} are between 0.8 and 0.9% for the doping range between 1 and 3%. Thus, we cannot exclude a slightly earlier onset of population of Mg on the Li site. The B_{iso} values are within a reasonable range observed in prior high-resolution PXRD studies of NCM materials.³⁰

Overall, the observed increase and then decrease in the Ni–O distance with increasing Mg^{2+} doping level can be either rationalized in a simple ionic model as an effect of the site occupancy on the formal Ni oxidation state or by considering the effect of doping on the band structure. In the ionic model with a fixed anionic O^{2-} lattice, doping with Mg_{Ni} induces an increase of the average Ni oxidation state for electroneutrality reasons (each $\text{Mg}_{\text{Ni}}^{2+}$ shall be compensated by a $\text{Ni}_{\text{Ni}}^{4+}$). This increase in the average oxidation state of Ni should lead to a smaller volume of the metal-oxide polyhedron as it slightly shifts the balance from the ionic radius of Ni^{3+} ($r = 0.56$ Å) to the smaller Ni^{4+} radius ($r = 0.48$ Å). However, this behavior is only observed for Mg contents < 2 mol%, as expected from the fact that oxidizing Ni beyond the trivalent state is challenging and can only be obtained under specific synthesis conditions.^{31,32} Once saturation of $\text{Mg}_{\text{Ni}}^{2+}$ is reached in the 1.7% sample (1.91(7) % as refined), the Mg_{Li} occupancy increases upon further Mg doping. As Mg_{Li} has the opposite, reducing effect on the formal Ni oxidation state (each $\text{Mg}_{\text{Li}}^{2+}$ shall be compensated by a $\text{Ni}_{\text{Ni}}^{2+}$; $r(\text{Ni}^{2+}) = 0.69$ Å), the average Ni oxidation state decreases again, leading to an increase in $d(\text{Ni–O})$. Compared to the Ni site, the Li site can host a higher fraction of Mg^{2+} ions without saturating. Thus, the Ni–O bond distance increases beyond the bond length observed in pristine LNO based on the partial reduction of the average Ni oxidation state away from the trivalent state. In the band-structure model, a shrinking of the Ni–O distance has been correlated to a downward shift of the Fermi level, a depopulation of the antibonding e_g^* states and an increase in the Ni–O bond covalence upon delithiation of LNO.^{33–36} Thus, Mg_{Ni} lowers the

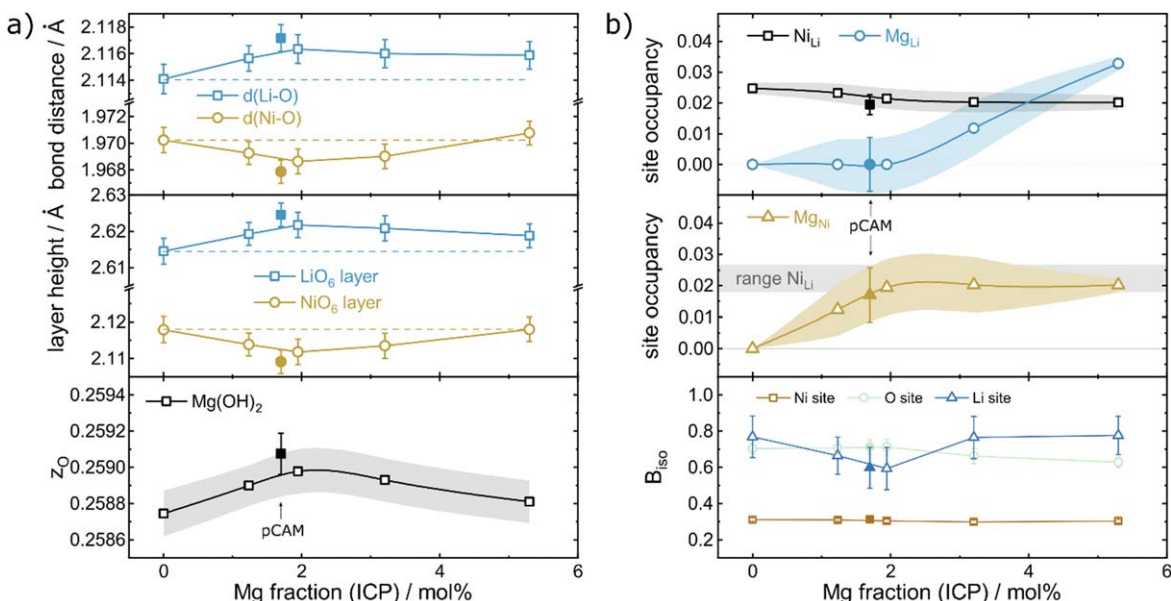


Figure 4. (a) Plots of the Li–O and Ni–O bond distance, layer height of the NiO_2 slab, and the interlayer space, and z_{O} vs the Mg doping fraction. (b) Fraction of the occupational defects of Ni_{Li} , Mg_{Li} , and Mg_{Ni} , as well as the B_{iso} values for each site in dependence of the Mg doping level.

Fermi level via hole doping, while Mg_{Li} leads to charge doping in the NiO_2 layer.

Electrochemistry.—As the structure is linked to the electrochemical properties of Mg-doped LNO, the powders were investigated as cathode tapes in coin half-cells. Cycling was performed between 3.0 and 4.3 V vs Li^+/Li at 25 °C. The rate was kept at C/10 for the first five cycles and then increased to 1C. The 56th and 107th cycles were performed at C/10 to test the capacity vs the values of the initial cycles. The results of these measurements are shown Figs. 4a–4d. There, the plot of the voltage vs specific capacity indicates a decreasing capacity with an increasing fraction of the electrochemically inactive Mg dopant from 228.4 mAh g^{-1} in LNO to 185.4 mAh g^{-1} in 5 mol% Mg-doped. However, one has to be cautious in comparing the absolute values, as there is a capacity increase during the first five cycles (see initial C/10 region). The capacity increase is more pronounced in samples with a high degree of doping and typically is associated with surface-related processes and the particles cracking over cycling.^{27,37,38} Additionally, the plateaus observed in the voltage profile of LNO, which are associated with phase transitions between structures with different Li^+ vacancy orderings,^{5,39} give way to sloping curves associated with solid-solution behavior at higher degrees of doping as seen in prior studies.¹²

The trend towards solid solution-like behavior with an increasing Mg fraction becomes more apparent in the differential capacity curves displayed in Fig. 4b. There, the expected hexagonal and monoclinic phase transitions of $\text{H1} \rightarrow \text{M} \rightarrow \text{M}' \rightarrow \text{M}'' \rightarrow \text{H2} \rightarrow \text{H3}$ are observed in the charging cycle of pristine LNO at 3.66, 3.77, 3.94, 4.02, and 4.19 V vs Li^+/Li .^{5,39} Once Mg is introduced, the peak intensities decrease with increasing degree of doping in the charge and discharge curve, again highlighting the change towards solid-solution behavior. The transitions $\text{M} \rightarrow \text{M}' \rightarrow \text{M}'' \rightarrow \text{H2}$ are either strongly suppressed ($\text{M} \rightarrow \text{M}'$, $\text{M}' \rightarrow \text{H2}$) or lost completely ($\text{M}'' \rightarrow \text{H2}$). The latter, in particular, is related to the structure $\text{Li}_{0.4}\text{NiO}_2$ and has been shown to be extremely sensitive to structural modifications.⁴⁰ In addition, the peak positions shift towards higher (lower) voltage with increasing Mg fraction during charging (discharging), indicating a thermodynamic change of the de-intercalation (intercalation) potential, in agreement with expectations.

The doping with Mg has a pronounced effect on the capacity and its retention, as expected based on prior studies,^{12,14} and displayed in

Fig. 5. The high initial specific discharge capacity of $q = 228 \text{ mAh g}^{-1}$ seen in pristine LNO decreases monotonically to 182 mAh g^{-1} with 5% Mg doping. Regardless of the site occupied, the dominant effect of the presence of Mg is thus a reduced available redox capacity, which like in most Ni-rich CAMs, can be expected to induce an improved cyclability. Mg doping also leads to a capacity activation within the first cycles, which is especially prevalent in samples with $\geq 1.7\%$ Mg. In confirmation of prior studies, the doping vastly improves the relative capacity retention at a 1C rate from 57% in the pristine compound to 73% in 5% Mg-doped LNO compared to the capacity of the 5th cycle. As the capacity retention is also rate dependent, it was determined as 71% for pristine LNO and 88% in 5% Mg-doped LNO in the 107th cycle vs the 5th cycle at a C/10 rate. These observations come as no surprise, since a lower state of charge (SOC) is reached for samples with higher Mg content, suggesting that processes, such as volume change and gas release, which are SOC dependent, are mitigated.

In order to relate the structure and electrochemical behavior, *operando* measurements were performed on the 3% Mg-doped LNO, which features a good balance between initial specific capacity, capacity retention, and low amount of doping. The cell was studied for three cycles, as can be seen in Fig. 6a. The observed phase transitions lead from the hexagonal (H1) to the monoclinic (M) phase in the CAM of the *operando* cell during delithiation, followed by a transition to the second hexagonal (H2) phase. The presence of the $\text{H2} \rightarrow \text{H3}$ transition usually observed in LNO was excluded, as the model yielded a higher R_{wp} value compared to a continuous volume contraction in the H2 phase. As expected, PXRD is sensitive to the motion of the Ni and O atoms relative to each other, as well as a change in the stacking height. The transition $\text{M} \rightarrow \text{M}'$ typical of LNO is not observed, as it is based on the ordering of the weak scatterer Li^+ . The behavior of the phase transitions is similar to the major peaks observed in the dq/dV data at 3.77 and 4.19 V, thus highlighting the similarity of the coin cell for electrochemical characterization to the cell used in the *operando* setup. Because of the limited quality of laboratory PXRD data, only single phases were refined, as two phase regions lead to large estimated standard deviations. Figure 6b highlights the 003 stacking reflection, as well as the 108 and 210 reflections, which evolve continuously during Li (de)intercalation. In pristine LNO, a volume collapse of the primitive unit cell from ~ 32.7 to $\sim 31.0 \text{ \AA}^3$ is observed during the transition from the $\text{H2} \rightarrow \text{H3}$ phase due to the sudden reduction

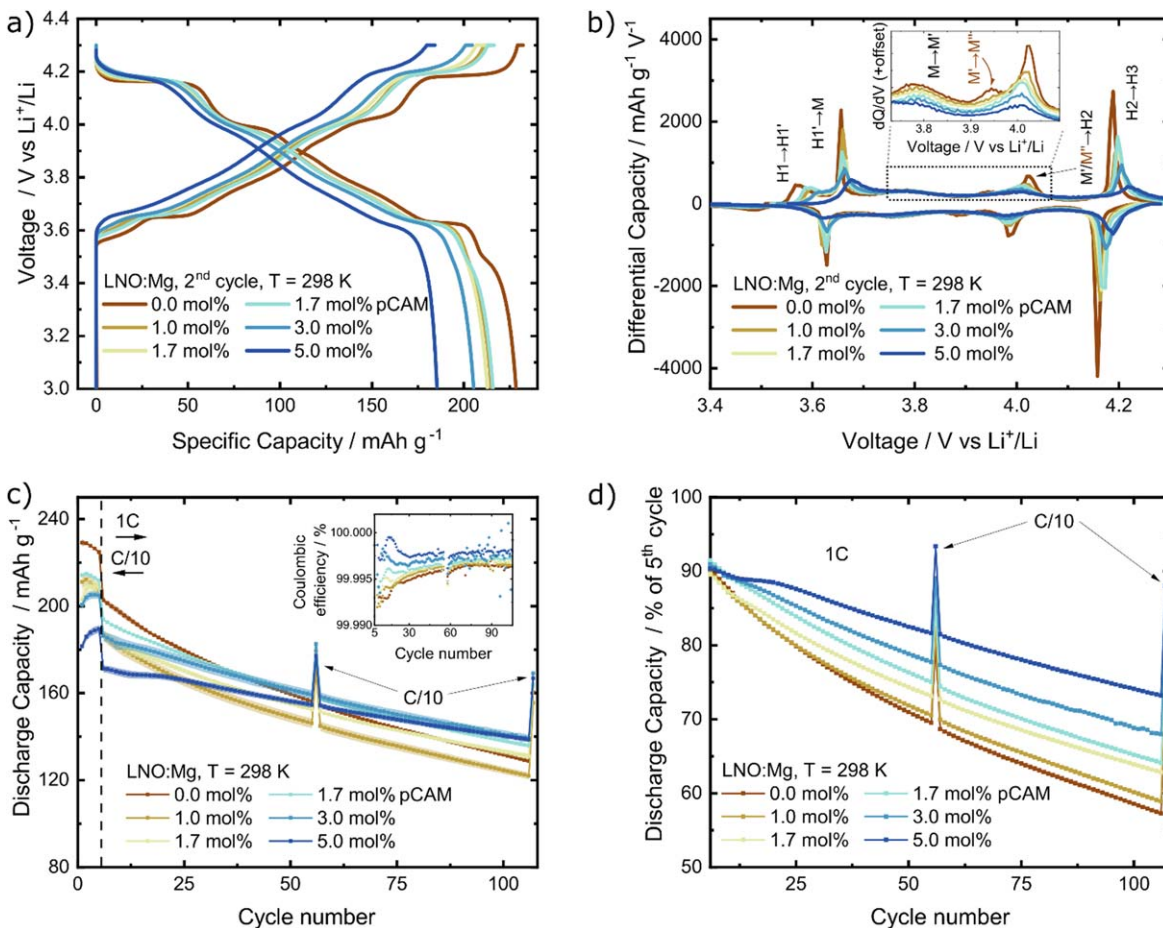


Figure 5. Galvanostatic data of half-cells cycled for undoped and Mg-doped LNO in the voltage range of 3.0–4.3 V vs Li^+/Li . (a) Voltage profiles and (b) plot of the differential specific capacity for the 2nd cycle of selected samples, (c) plot of the specific discharge capacity in mAh g^{-1} with error bands and an inset showing the Coulombic efficiency, and (d) plot of discharge capacity as % of the 5th cycle.

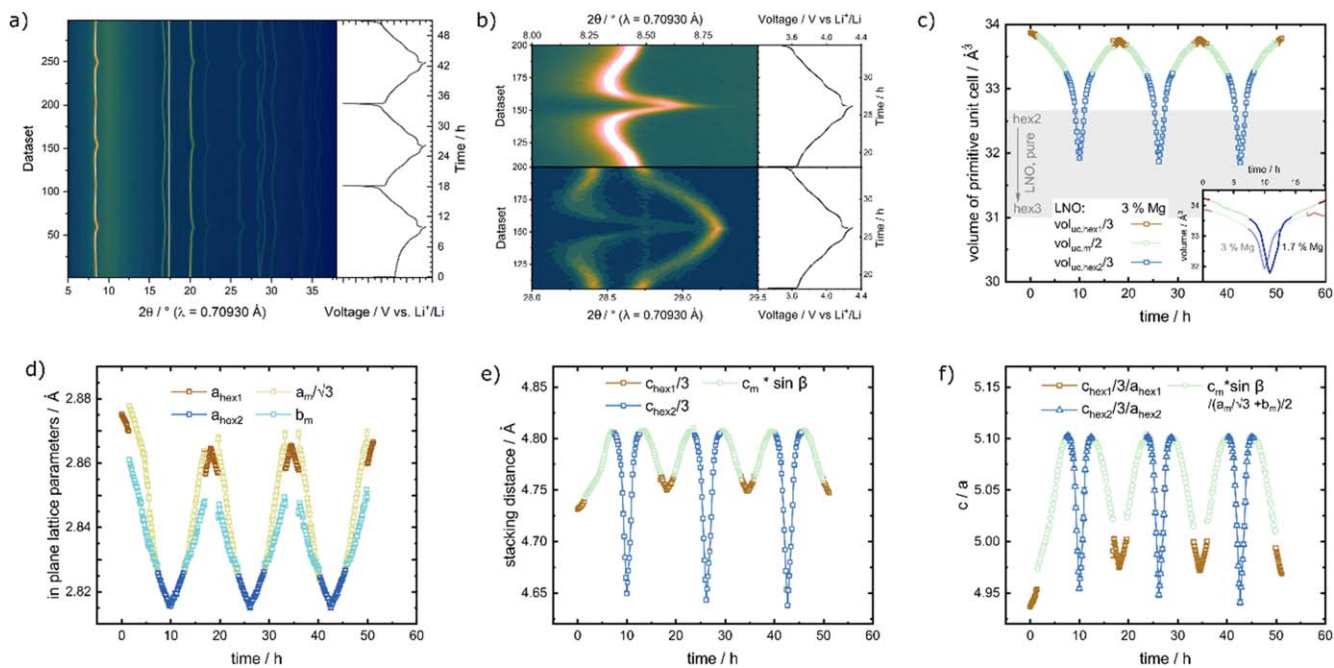


Figure 6. (a) Contour plots of the diffraction patterns and voltage vs time profiles of the *operando* PXRD measurement of 3% Mg-doped LNO. (b) Zoomed contour plots (2θ regions of 8–9° and 28–29.5°) of the 003 (upper) and 108/210 reflection in the second cycle. Time evolution of (c) the volume of the primitive unit cell (inset comparing the volume change in 1st cycle of the 1.7 vs 3% Mg sample), (d) in-plane lattice parameter, (e) stacking distance, and (f) c/a ratio.

of the interlayer space. This behavior is not observed in the 3% Mg-doped sample, thereby leading to mitigated mechanical stresses in the cathode composite and to a higher capacity retention during cycling. The material thus features solid-solution behavior rather than a distinct H2 → H3 phase transformation. The total volume change of $\Delta V/V = -10.5\%$ in pristine LNO³⁹ is larger than $\Delta V/V = -5.7\%$ in 3 mol% Mg-doped LNO, whose change of the unit cell volume is continuous. We also verified the *operando* behavior of the 1.7% Mg-doped sample. It shows single-phase behavior in the highly delithiated state up to 4.3 V, with a slightly more pronounced volume contraction of $\Delta V/V = -7.1\%$ between the unit cell volumes of the charged and discharged material, see Fig. 6c. This indicates that, even when Mg at low concentration occupies the Ni site, it improves the mechanical behavior of the cathode by reducing the volume change and the stressful biphasic reactions. The volume decrease during delithiation is driven by the average in-plane lattice parameter, as displayed in Figs. 6c, 6d. There, the monoclinic lattice parameter $a_m/\sqrt{3}$ is used for comparability to the hexagonal lattice parameter a_{hex} . In contrast to the lattice parameter a , the layer stacking distance first increases during delithiation, then decreases once the M → H2 transition is reached (Fig. 6e). Its evolution then affects the c/a ratio, as seen in Fig. 6f. Future experiments utilizing *operando* synchrotron XRD and more local techniques could be used to test the role of Mg into more advanced models such as those including stacking faults³⁹ or Nickel on the tetrahedral 6c site.⁴¹

Conclusions

In this study, we investigated the interplay between crystallographic structure and electrochemistry of Mg(OH)₂ nanoparticle-doped LNO in the Mg doping range 0–5 mol%. First, we establish that mixtures of Ni(OH)₂ with 10 nm small nanoparticles of Mg(OH)₂ enable the synthesis of single-phase, homogeneously doped materials, similar to samples prepared from co-precipitated reactants. Unlike in prior studies based on laboratory PXRD data only, the use of high-resolution synchrotron PXRD data reveals clear trends in the low doping regime. In particular, we show that Mg occupies the Ni site up until ~2%, and only then starts to occupy the Li site. Additionally, the occupancies correlate with observable Ni–O bond lengths. Hence, the location of Mg in LNO is not straightforward and its proper location is of importance to understand its effect, and even more important for modeling efforts in the literature. Electrochemical testing as a CAM in coin half-cells shows that with increasing doping concentration, the capacity retention increases at the expense of the initial specific capacity, comparable to other studies on the effect of Mg in LNO. This can be related to the lower effective SOC reached during cycling, as well as to the structural stabilization brought by the Mg dopant, resulting in a smoother voltage curve with less phase transition and lower volume change upon cycling. This weakening of the H2–H3 transition has been associated with less particle cracking.⁴²

As current technology trends towards higher degrees of Ni in CAMs, stabilization needs to originate from ever-lower degrees of dopants. Thus, the presented work sheds light on technologically relevant high-Ni cathode active materials and improves the understanding of structure-property relationships in the low doping regime.

Acknowledgments

This study was supported by BASF SE. Some of the experiments were performed at the Materials Science and Powder Diffraction beamline (BL04) at ALBA Synchrotron with the collaboration of ALBA staff. François Fauth is acknowledged for his continuous support. We thank Dr. Thomas Bergfeldt (IAM, KIT) for ICP-OES measurements.

ORCID

Daniel Weber  <https://orcid.org/0000-0003-4175-9278>

Jürgen Janek  <https://orcid.org/0000-0002-9221-4756>
Torsten Brezesinski  <https://orcid.org/0000-0002-4336-263X>
Matteo Bianchini  <https://orcid.org/0000-0003-4034-7706>

References

- G. E. Blomgren, *J. Electrochem. Soc.*, **164**, A5019 (2017).
- C. S. Yoon, M. H. Choi, B.-B. Lim, E.-J. Lee, and Y.-K. Sun, *J. Electrochem. Soc.*, **162**, A2483 (2015).
- W. Li, E. M. Erickson, and A. Manthiram, *Nat. Energy*, **5**, 26 (2020).
- N. Li, S. Sallis, J. K. Papp, J. Wei, B. D. McCloskey, W. Yang, and W. Tong, *ACS Energy Lett.*, **4**, 2836 (2019).
- M. Bianchini, M. Roca-Ayats, P. Hartmann, T. Brezesinski, and J. Janek, *Angew. Chem. Int. Ed.*, **58**, 10434 (2019).
- U.-H. H. Kim et al., *Energy Environ. Sci.*, **11**, 1271 (2018).
- F. Kong, C. Liang, L. Wang, Y. Zheng, S. Peranathan, R. C. Longo, J. P. Ferraris, M. Kim, and K. Cho, *Adv. Energy Mater.*, **9**, 1802586 (2019).
- L. Mu et al., *J. Mater. Chem. A*, **8**, 17487 (2020).
- L. de Biasi, A. Schiele, M. Roca-Ayats, G. Garcia, T. Brezesinski, P. Hartmann, and J. Janek, *ChemSusChem*, **12**, 2240 (2019).
- C. S. Yoon, D.-W. Jun, S.-T. Myung, and Y.-K. Sun, *ACS Energy Lett.*, **2**, 1150 (2017).
- H. Li, M. Cormier, N. Zhang, J. Inglis, J. Li, and J. R. Dahn, *J. Electrochem. Soc.*, **166**, A429 (2019).
- C. Poullierie, L. Croguennec, P. Biensan, P. Willmann, and C. Delmas, *J. Electrochem. Soc.*, **147**, 2061 (2000).
- A. Liu, N. Zhang, H. Li, J. Inglis, Y. Wang, S. Yin, H. Wu, and J. R. Dahn, *J. Electrochem. Soc.*, **166**, A4025 (2019).
- R. Sathiyamoorthi, P. Shakkthivel, S. Ramalakshmi, and Y. G. Shul, *J. Power Sources*, **171**, 922 (2007).
- M. M. E. Cormier, N. Zhang, A. Liu, H. Li, J. Inglis, and J. R. Dahn, *J. Electrochem. Soc.*, **166**, A2826 (2019).
- A. Liu, N. Zhang, J. E. Stark, P. Arab, H. Li, and J. R. Dahn, *J. Electrochem. Soc.*, **168**, 050506 (2021).
- A. Liu, N. Zhang, J. E. Stark, P. Arab, H. Li, and J. R. Dahn, *J. Electrochem. Soc.*, **168**, 040531 (2021).
- C. Poullierie, L. Croguennec, and C. Delmas, *Solid State Ionics*, **132**, 15 (2000).
- L. Mu, W. H. Kan, C. Kuai, Z. Yang, L. Li, C. J. Sun, S. Sainio, M. Avdeev, D. Nordlund, and F. Lin, *ACS Appl. Mater. Interfaces*, **12**, 12874 (2020).
- L. Mu et al., *Chem. Mater.*, **31**, 9769 (2019).
- W. Mo Seong and A. Manthiram, *ACS Applied Materials & Interfaces*, **12**, 43653 (2020).
- J. Cheng, L. Mu, C. Wang, Z. Yang, H. L. Xin, F. Lin, and K. A. Persson, *J. Mater. Chem. A*, **8**, 23293 (2020).
- R. D. Shannon, *Acta Crystallogr., Sect. A*, **32**, 751 (1976).
- F. Fauth, R. Boer, F. Gil-Ortiz, C. Popescu, O. Vallcorba, I. Peral, D. Fullà, J. Benach, and J. Juanhuix, *The European Physical Journal Plus*, **130**, 160 (2015).
- F. Fauth, I. Peral, C. Popescu, and M. Knapp, *Powder Diffr.*, **28**, S360 (2013).
- R. E. Dinnebier, A. Leineweber, and J. S. O. Evans, *Rietveld Refinement: Practical Powder Diffraction Pattern Analysis Using TOPAS* (De Gruyter, Berlin/Boston) (2018).
- D. Kutsche, S. Schweidler, A. Mazilkin, H. Geßwein, F. Fauth, E. Suard, P. Hartmann, T. Brezesinski, J. Janek, and M. Bianchini, *Materials Advances*, **1**, 639 (2020).
- T. M. Sabine, B. A. Hunter, W. R. Sabine, and C. J. Ball, *J. Appl. Crystallogr.*, **31**, 47 (1998).
- D. Weber, K. Tripković, M. Kretschmer, and T. B. Bianchini, *Eur. J. Inorg. Chem.*, **2020**, 3117 (2020).
- L. Yin et al., *Rev. Sci. Instrum.*, **89**, 093002 (2018).
- M. Bianchini et al., *Chem. Mater.*, **32**, 9211 (2020).
- A. Mesnier and A. Manthiram, *ACS Appl. Mater. Interfaces*, **12**, 52826 (2020).
- I. Nakai, K. Takahashi, Y. Shiraiishi, T. Nakagome, and F. Nishikawa, *J. Solid State Chem.*, **140**, 145 (1998).
- W. S. Yoon, K. Y. Chung, J. McBreen, D. A. Fischer, and X. Q. Yang, *J. Power Sources*, **163**, 234 (2006).
- S. Laubach, S. Laubach, P. C. Schmidt, D. Enslin, S. Schmid, W. Jaegermann, A. Thißen, K. Nikolowski, and H. Ehrenberg, *Phys. Chem. Chem. Phys.*, **11**, 3278 (2009).
- M. K. Aydinol, A. F. Kohan, G. Ceder, K. Cho, and J. Joannopoulos, *Physical Review B*, **56**, 1354 (1997).
- R. Ruess, S. Schweidler, H. Hemmelmann, G. Conforto, A. Bielefeld, D. A. Weber, J. Sann, M. T. Elm, and J. Janek, *J. Electrochem. Soc.*, **167**, 100532 (2020).
- F. Riewald, P. Kurzhals, M. Bianchini, H. Sommer, J. Janek, and H. A. Gasteiger, *J. Electrochem. Soc.*, **169**, 020529 (2022).
- M. Mock, M. Bianchini, F. Fauth, K. Albe, and S. Siculo, *J. Mater. Chem. A*, **9**, 14928 (2021).
- P. Kurzhals, F. Riewald, M. Bianchini, H. Sommer, H. A. Gasteiger, and J. Janek, *J. Electrochem. Soc.*, **168**, 110518 (2021).
- N. Ikeda, I. Konuma, H. B. Rajendra, T. Aida, and N. Yabuuchi, *J. Mater. Chem. A*, **9**, 15963 (2021).
- A. O. Kondrakov, A. Schmidt, J. Xu, H. Geßwein, R. Mönig, P. Hartmann, H. Sommer, T. Brezesinski, and J. Janek, *The Journal of Physical Chemistry C*, **121**, 3286 (2017).